ACCSCIENCE PUBLISHING

Materials Science in Additive Manufacturing

ORIGINAL RESEARCH ARTICLE

Uncovering the role of heterogeneous microstructure in the mechanical anisotropy of ultra-high-strength steel fabricated by directed energy deposition–arc

Junyang Tu, Mingjie Zhao*, Lihong Jiang, You Li, An Lu, and Zhenghua Guo

Jiangxi Provincial Key Laboratory of Extreme Manufacturing Technology for High-end Equipment, School of Materials Science and Engineering, Nanchang Hangkong University, Nanchang, Jiangxi, China

***Corresponding author:**
Mingjie Zhao
(zhaomj@nchu.edu.cn)

Citation: Tu J, Zhao M, Jiang L, Li Y, Guo Z. Uncovering the role of heterogeneous microstructure in the mechanical anisotropy of ultra-high-strength steel fabricated by directed energy deposition–arc. *Mater Sci Add Manuf*. 2026;5(3):026240055. doi: 10.36922/MSAM026240055

Received: June 9, 2026

Revised: July 3, 2026

Accepted: July 8, 2026

Published online: July 21, 2026

Copyright: © 2026 Author(s). This is an Open-Access article distributed under the terms of the Creative Commons Attribution License, permitting distribution, and reproduction in any medium, provided the original work is properly cited.

Publisher's Note: AccScience Publishing remains neutral with regard to jurisdictional claims in published maps and institutional affiliations.

Abstract

The anisotropic properties of components produced by directed energy deposition–arc (DED-Arc) markedly limit their use in engineering. Thus, it is crucial to elucidate the mechanism that regulates this anisotropic phenomenon in DED-Arc components to ensure the reliable application of this technology in high-performance components. In this study, 300M steel was fabricated by DED-Arc with controlled interlayer temperature, and a critical phenomenon was observed. At an interlayer temperature of 200 °C, the strength was isotropic, while the ductility exhibited a certain degree of anisotropy. When the interlayer temperature increased above the martensite start temperature to 300 °C, a unique anisotropy in mechanical properties emerged. The vertical specimens exhibited higher ultimate tensile strength and elongation but lower yield strength than the horizontal specimens. At an interlayer temperature of 200 °C, the microstructure was relatively uniform and consisted entirely of tempered martensite. The plastic anisotropy mainly originated from directional grain growth. At an interlayer temperature of 300 °C, the microstructure evolved into a heterogeneous structure consisting of alternating soft and hard zones, caused by the uneven distribution of soft phases (tempered martensite and needle like bainite) and hard phases (untempered martensite). In this case, the spatial arrangement of the heterogeneous structure governed the anisotropy. Under horizontal tension, the soft and hard zones are alternately stacked perpendicular to the tensile direction, and the deformation compatibility was constrained by the hard zones, resulting in higher yield strength but lower ductility. Under vertical tension, the soft and hard zones are stacked parallel to the tensile direction, offering better deformation compatibility. Moreover, the Orowan strengthening effect induced by the interlayer regions was more pronounced, leading to a higher ultimate tensile strength than that of the horizontal specimens. This study elucidates the microscale mechanism of heterogeneous structure formation upon exceeding the martensite start temperature, thereby producing this unique anisotropy.

Keywords: Ultra-high-strength steel; Directed energy deposition; Interlayer temperature; Heterogeneous structure; Anisotropy

1. Introduction

Due to its outstanding combination of properties that meet strict service demands, ultra-high-strength steel (UHSS) is extensively applied in large and complex components within advanced sectors such as aerospace and nuclear power.[1-3] Nevertheless, the production of such large and complex components through traditional methods is hindered by extended production cycles, inefficient material usage, and high costs.[4] As an important branch of additive manufacturing technology, directed energy deposition (DED)–arc (DED-Arc) uses an electric arc as the heat source to achieve near-net-shape fabrication of three-dimensional complex components through layer-by-layer melting and stacking.[5,6] With features such as a fast deposition rate, high material utilization, good environmental adaptability, and manufacturing flexibility, DED-Arc has emerged as one of the most promising technologies for the fabrication of large and complex components in advanced manufacturing.[7-9]

Currently, the application of DED-Arc technology to UHSS has attracted considerable attention. Guo *et al.* [10] investigated the microstructural transformation of DED–plasma arc (DED-PA) UHSS under different thermal cycles, and revealed that the bainite transformation mode follows a superledge growth mechanism. Zhang *et al.*[11] investigated 18Ni 300 maraging steel fabricated by DEDArc under different modes and found that the low heat input in the cold metal transfer (CMT) mode facilitates the formation of a {110}<001> Goss texture, which yields the best mechanical properties. Lyu *et al.*[12] found that controlling the interlayer temperature to regulate the intrinsic heat treatment during the DED-Arc process is an effective strategy to synergistically enhance the strength and ductility of 17-4PH steel. Xiong *et al.*[13] developed an enhanced heat treatment procedure for DED-Arc 300M steel, achieving mechanical properties that exceed those of the forged counterpart. Li *et al.*[14] found that a novel heat treatment strategy involving quenching, tempering, and deep cryogenic treatment can effectively mitigate the strength–ductility trade-off in DED-PA UHSS.

While DED-Arc technology has demonstrated notable promise in producing UHSS components, the majority of existing research has concentrated on optimizing the process, studying microstructural changes, improving mechanical properties, and exploring heat treatment.[4] However, insufficient consideration has been given to the anisotropy of mechanical properties. In fact, the notable temperature gradient and non-uniform solidification inherent in the DED-Arc process lead to the microstructural evolution of the as-deposited component, inevitably causing anisotropy in mechanical properties.[15] The mechanical anisotropy often leads to premature failure along the weaker directions, severely restricting engineering applications.[16] Thus, in addition to the research directions outlined above, it is crucial to thoroughly investigate the dominant mechanisms that govern the mechanical anisotropy of DED-Arc components.

Several researchers attribute the mechanical anisotropy of DED-Arc components primarily to the directional growth of columnar grains induced by a notable thermal gradient, which creates a strong texture. Shi *et al.*[17] examined TC4 produced through DED-PA and discovered that its hierarchical microstructure, which includes large prior β columnar grains aligned along the build direction, markedly affects its mechanical anisotropy. Blinn *et al.*[18] found that the combined effect of a strong texture, δ-ferrite dendrites growing along the build direction, and elongated grains leads to the anisotropic deformation behavior of DED-Arc austenitic stainless steel. Akbarzadeh Chiniforoush *et al.*[19] demonstrated that the use of a reciprocating strategy can effectively hinder the growth of columnar grains in DED–gas metal arc (DED-GMA) of duplex stainless steel, thereby reducing mechanical anisotropy. Palmeira Belotti *et al.*[20] reported that mechanical anisotropy in DED-Arc 316LSi stainless steel is closely linked to crystallographic texture. The highest macroscopic yield strength (YS) is achieved when the load is applied along the <111> crystal direction.

Additionally, several studies have attributed the mechanical anisotropy to microstructural heterogeneity arising from non-uniform tempering of previously deposited layers. Sun *et al.*[21] reported that in DED-CMT low-carbon steel, different thermal histories lead to distinct microstructural features between the intralayer and interlayer regions. The interlayer regions serve as weak zones, accounting for the lower longitudinal mechanical properties compared to the transverse direction. Chen *et al.*[22] reported that in DED-CMT reduced activation ferritic/martensitic steel, the heterogeneous structure composed of alternating heat-affected zones, columnar grain zones, and fine-grained zones results in mechanical anisotropy. Tu *et al.*[23] reported that in the DED-Arc GW123K alloy featuring a lamellar heterogeneous structure, the crack propagation paths differ among tensile specimens tested in different directions, which results in anisotropic mechanical properties. Lyu *et al.*[24] revealed that tailoring the heterogeneous distribution of tempered martensite (TM) and elongated δ-ferrite phases effectively mitigates the mechanical anisotropy of DED-CMT martensitic stainless steel. Texture and heterogeneous structure commonly coexist and are often interconnected in the DED-Arc process. However, few studies have addressed both factors simultaneously.

The present study utilized DED-Arc technology to fabricate 300M steel, a typical UHSS, by controlling the interlayer temperature below and above the martensite start temperature (Ms). By comparing the mechanical anisotropy associated with different microstructural features, this study aims to clarify the respective influences of texture and heterogeneous structure on the mechanical anisotropy of DEDArc 300M steel and to identify the dominant mechanisms under different microstructural conditions. This work provides a theoretical basis for the proactive tailoring of mechanical properties in DED-Arc UHSS.

2. Materials and methods

2.1. Materials

In this study, 300M steel powder (Liaoning Guanda New Material Technology Co., Ltd., China) with a particle size of 53–150 μm was used. The substrate material was 316L stainless steel (Xinghua Jiazhiyuan Stainless Steel Products Co., Ltd., China) with dimensions of 100 mm × 150 mm × 10 mm. The chemical composition of the DED-Arc component was measured by inductively coupled plasma mass spectrometry (Agilent Technologies, USA) and an organic elemental analyzer (LECO Corporation, USA), yielding the following composition (in wt.%): 0.37 C, 1.47 Si, 0.83 Mn, 0.84 Cr, 0.44 Mo, 1.71 Ni, 0.077 V, 0.014 Cu, and the balance Fe.

2.2. Experimental process

The deposition experiment was conducted on a powderfed DED-Arc system, which consists of a KR30HA highprecision sixaxis robot and a EuTronic® GAP 2501 DC plasma arc welding system. The welding torch was mounted at the front end of the robot, which precisely controlled the additive path to ensure deposition stability. The torch moved unidirectionally along the *Y*-axis on the substrate during the deposition process, building up layer by layer along the *Z*-axis. A K-type thermocouple was employed to monitor the interlayer temperature variation.

A previous study has revealed that an interlayer temperature exceeding 350 °C during DED-Arc of high-strength steel can cause the collapse of the deposited layer.[25] Considering factors such as forming quality and phase transformation temperature, specimens with 20 deposited layers were fabricated at interlayer temperatures of 200 °C and 300 °C, respectively. The procedure involved controlling the interlayer temperature of each deposited layer to remain below or above the Ms. After depositing each layer, the arc was extinguished, and the temperature was measured on the deposited layer surface using a contact-type K-type thermocouple. The component was then air-cooled to the target interlayer temperature before depositing the next layer. The schematic diagram of the DED-Arc process is shown in Figure 1A. The processing parameters were as follows: a current of 160 A, a deposition speed of 0.14 m/min, and a powder feeding rate of 15 g/min. The shielding gas, powder feeding gas, and plasma gas were all high-purity argon (99.99%), with flow rates of 15 L/min, 3 L/min, and 1.5 L/min, respectively.

2.3. Microstructure characterization and mechanical properties tests

Metallographic specimens, as well as horizontal and vertical tensile specimens, were extracted from the deposited component by wire electrical discharge machining. The sampling locations and dimensions of the tensile specimens are shown in Figure 1B. The specimens were ground and mechanically polished, then etched with a 4% nital solution. The microstructures were observed using optical microscopy (OLYMPUS, Japan) and field-emission scanning electron microscopy (CIQTEK Quantum Technology Co., Ltd., China). After electropolishing, electron backscatter diffraction (EBSD) was performed. Vickers hardness tests were carried out under a load of 48.0 N with a dwell time of 15 s. For each DED-Arc component, 10 indentations were performed along the build direction (*Z*-axis) with a spacing of 0.25 mm, covering both the interlayer and intralayer regions. Room-temperature tensile tests were conducted on a universal testing machine at a tensile speed of 0.18 mm/min using the specimen dimensions shown in Figure 1C. The fracture morphologies were observed by scanning electron microscopy (CIQTEK Quantum Technology Co., Ltd., China).

3. Results and discussion

3.1. Microstructural characteristics

Based on the measured chemical composition, the continuous cooling transformation curve for 300M steel was calculated using JMatPro software (version 7.0, Sente Software Ltd., UK), and the resulting diagram is illustrated in Figure 2. The findings revealed that the austenitization temperature of 300M steel is 827.87 °C, and the Ms is 289.5 °C. The bainite transformation temperature range is 301.87 °C –464.87 °C, with a cooling rate of less than 10°C/s. The pearlite transformation temperature range is 514.87 °C–723.87 °C, with a cooling rate of less than 1 °C/s.

Owing to the rapid cooling and reheating characteristics of the DED-Arc process, the formation of pearlite in DED-Arc 300M steel components is highly unlikely.[26] Based on Figure 2, at an interlayer temperature of 300 °C,

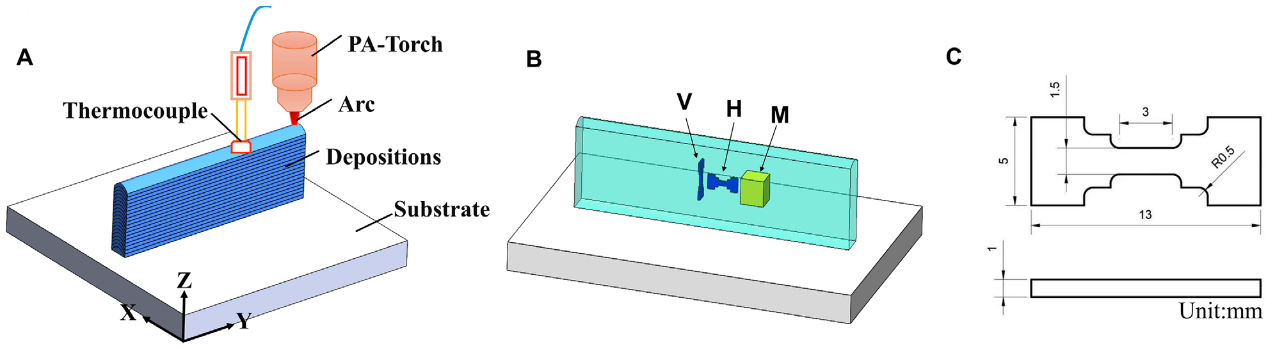

Figure 1. Directed energy deposition–arc (DED-Arc) process and sampling positions. (A) Schematic diagram of the DED-Arc process, (B) sampling positions, and (C) dimensions of the tensile specimen.

Abbreviations: H: Horizontal; M: Metallographic; PA: Plasma; V: Vertical.

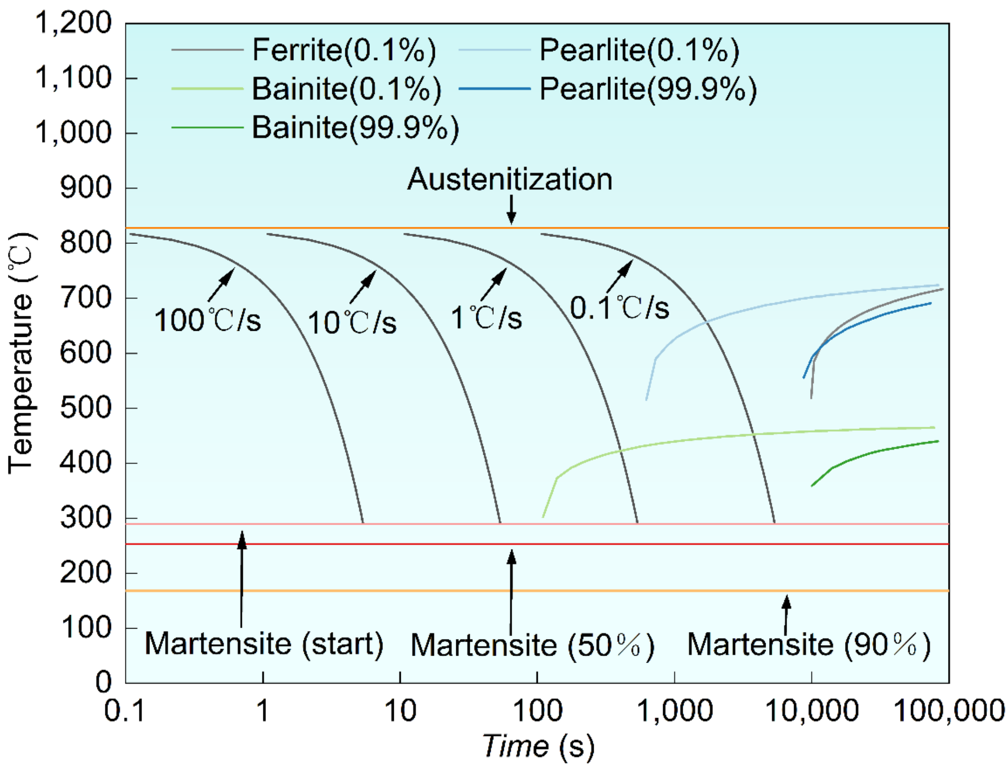

Figure 2. Continuous cooling transformation curve of the 300M steel

this temperature is approximately 10.5 °C higher than Ms (289.5 °C), while the interlayer temperature of 200 °C is far below Ms.

Figure 3 illustrates the microstructural features at different interlayer temperatures. A mixture of equiaxed and elongated columnar grains is observed at 200 °C, as shown in Figure 3A. At 300°C, coarse columnar grains are evident, as shown in Figure 3B. When the interlayer temperature is higher, the temperature gradient between adjacent layers becomes smaller, and the solidification rate becomes lower. Columnar grains are more likely to form when the temperature gradient is high, and the solidification rate is low.[27] Moreover, a higher interlayer temperature leads to a slower cooling rate, thereby promoting grain coarsening.[28]

During the DED-Arc process, the microstructure in previously deposited layers is affected by the thermal cycles of subsequent depositions. If the peak temperature exceeds the austenitization temperature, the microstructure reverts to austenite and rapidly transforms into untempered martensite (UTM) upon subsequent cooling. If the peak temperature falls below the austenitization temperature, the previously formed martensite undergoes tempering.[29] When the interlayer temperature is 200 °C, the martensite mainly undergoes low-temperature tempering (250 °C –310 °C). When the interlayer temperature is 300 °C, the martensite mainly undergoes high-temperature tempering (>310 °C). Based on previous studies, it is known that during low-temperature tempering, dispersed carbides (DC) are primarily precipitated, whereas during high-temperature tempering, cementite (CM), which is incoherent with the matrix, is predominantly precipitated.[10,30] Therefore, at an interlayer temperature of 200 °C, the microstructure is mainly composed of TM, as shown in Figure 3C, with DC as the primary precipitate. When the interlayer temperature exceeds the Ms, austenite does not directly transform into martensite; instead, it partially transforms into bainite within the bainite transformation temperature range.[31] When the interlayer temperature is 300 °C, it exceeds Ms. Due to the relatively rapid cooling rate, the bainite transformation is incomplete, and only a fraction of needle-like bainite (NLB) is formed. Most of the retained austenite transforms into UTM after the deposition process.[32] Therefore, at an interlayer temperature of 300 °C, the microstructure is composed of UTM, TM, and NLB, as shown in Figure 3D, with CM as the primary precipitate.

Figure 4 illustrates the EBSD results at different interlayer temperatures. Figure 4A and 4D are the inverse pole figures at interlayer temperatures of 200 °C and 300 °C, respectively. It can be observed that martensite grows epitaxially along the build direction, with a consistent orientation within the same martensite lath group. When the interlayer temperature increases from 200 °C to 300 °C, the degree of tempering is enhanced, leading to an increase in the martensite lath size. At 300 °C, bainite is observed to penetrate through the martensite lath group, thereby refining the microstructure.

Figure 4B and 4E illustrate the corresponding phase maps. At both interlayer temperatures, the retained austenite content is below 0.5%. Due to the rapid cooling characteristic of the DED-Arc process, the austenite almost completely transforms upon cooling after deposition, regardless of the interlayer temperature. Figure 4C and 4F present the kernel average misorientation (KAM) maps. KAM is related to the geometrically necessary dislocation (GND) density, and the relationship is as follows:[33]

$$\rho_{\mathrm{GND}} = \frac{2KAM_{\mathrm{avg}}}{\mu \mathrm{b}} \tag{1}$$

where ρ_{GND} is the GND density, KAM_{avg} is the average KAM, μ is the step size, and b is the Burgers vector.

Based on **Equation 1**, a higher KAM value corresponds to a higher GND density. As the interlayer temperature increases from 200 °C to 300 °C, the dislocation density decreases. During cooling, a high density of dislocations is generated to accommodate lattice contraction.[34] At an interlayer temperature of 200 °C, the cooling time is longer, and the cooling rate is faster, resulting in a higher dislocation density.

Figure 4G and 4H illustrate the pole figures at interlayer temperatures of 200 °C and 300 °C, respectively. It is generally accepted that when the texture intensity exceeds 5, the material can be considered to exhibit a strong texture.[35] The maximum texture intensities at the two interlayer temperatures are 10.93 and 13.70, respectively, indicating that both samples exhibit a strong texture with the maximum pole density at the {100} orientation. Meanwhile, the pole figures indicate texture orientations in various directions. This texture characteristic and its preferred orientation affect the mechanical anisotropy of the DED-Arc components.

3.2. Regional microstructural differences

Figure 5 illustrates the microstructures of the intralayer and interlayer regions at different interlayer temperatures. During the deposition process, high-temperature molten metal is transferred to previously deposited areas, leading to localized remelting. The region near the solid–liquid interface, adjacent to the molten pool, undergoes sufficient tempering and exhibits substantial thermal influence. This region is known as the interlayer region. In contrast, the region far from the molten pool undergoes lowtemperature tempering to a lesser extent and is therefore defined as the intralayer region.[21]

When the interlayer temperature is 200 °C, each layer undergoes martensitic transformation during cooling. Owing to the low interlayer temperature, the peak temperature in the middle region during subsequent deposition tends to fall below the austenitization temperature. Consequently, both the interlayer and intralayer regions undergo sufficient tempering, resulting in a microstructure composed entirely of TM. However, when the interlayer temperature reaches 300 °C, there is a substantial difference between the microstructures of the interlayer and intralayer regions, with a higher degree of tempering observed in the interlayer region.

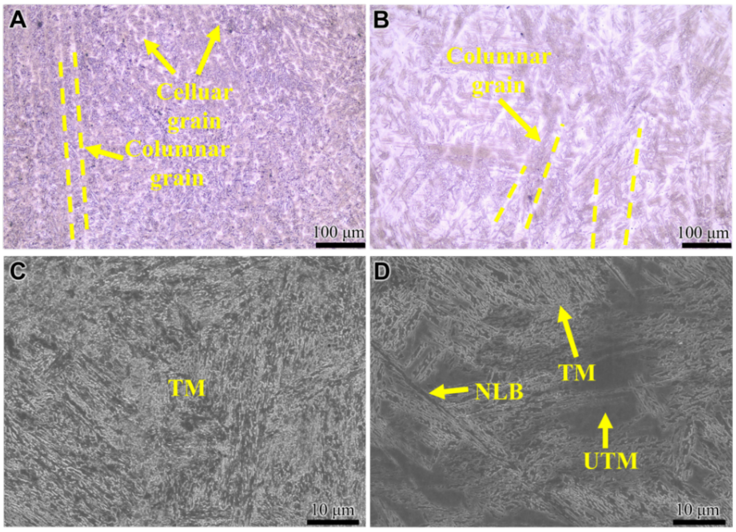

Figure 3. Microstructural features at different interlayer temperatures. (A,B) Optical microscopy images at (A) 200 °C and (B) 300 °C (scale bar = 100 μm; magnification = 200×). (C,D) Scanning electron microscopy images at (C) 200 °C and (D) 300 °C (scale bar = 10 μm; magnification = 2,000×). Abbreviations: NLB: Needle-like bainite; TM: Tempered martensite; UTM: Untempered martensite.

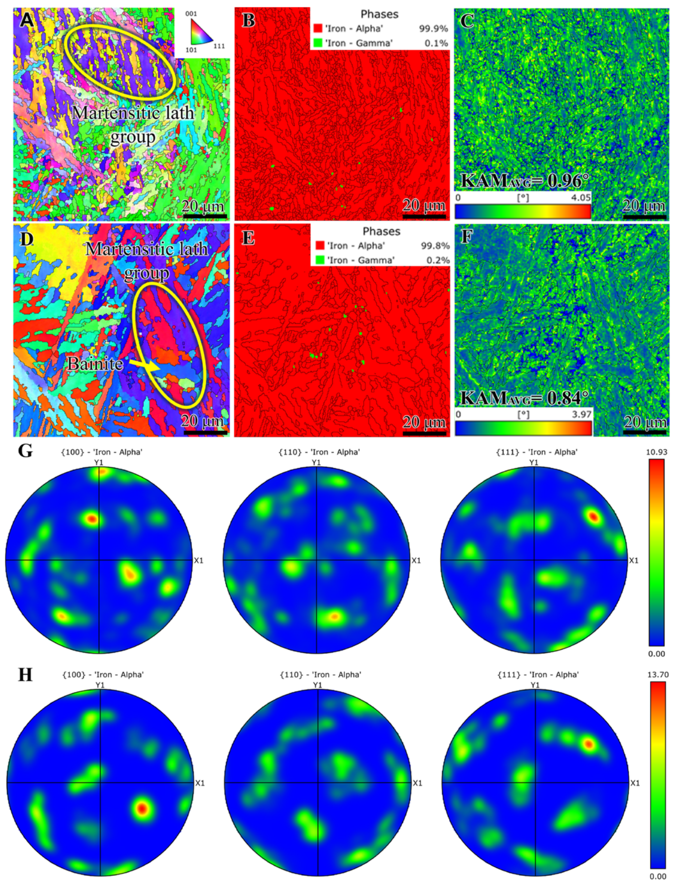

Figure 4. Electron backscatter diffraction results of samples fabricated at interlayer temperatures of 200 °C and 300 °C. (A–C) Inverse pole figure, phase map, and kernel average misorientation (KAM) map at 200 °C (scale bar = 20 μm; magnification = 1,500×). (D–F) Inverse pole figure, phase map, and KAM map at 300 °C (scale bar = 20 μm; magnification = 1,500×). (G, H) Pole figures of the (G) 200 °C and (H) 300 °C samples.

Image analysis using Image Pro Plus 6.0 (Media Cybernetics, Inc., USA) showed that the proportion of UTM in the intralayer region is 39.00% (Figure 5E), which is markedly higher than that in the interlayer region (21.82%; Figure 5F). In both regions, NLB is observed to separate UTM regions. To further quantitatively analyze the difference in the degree of tempering between the interlayer and intralayer regions at 300 °C, the precipitated CM in the two regions was statistically analyzed, as shown in Figure 5G and 5H. The quantitative analysis results are shown in Figure 5I and 5J. The volume fraction of CM in the interlayer region is 1.22%, which is markedly higher

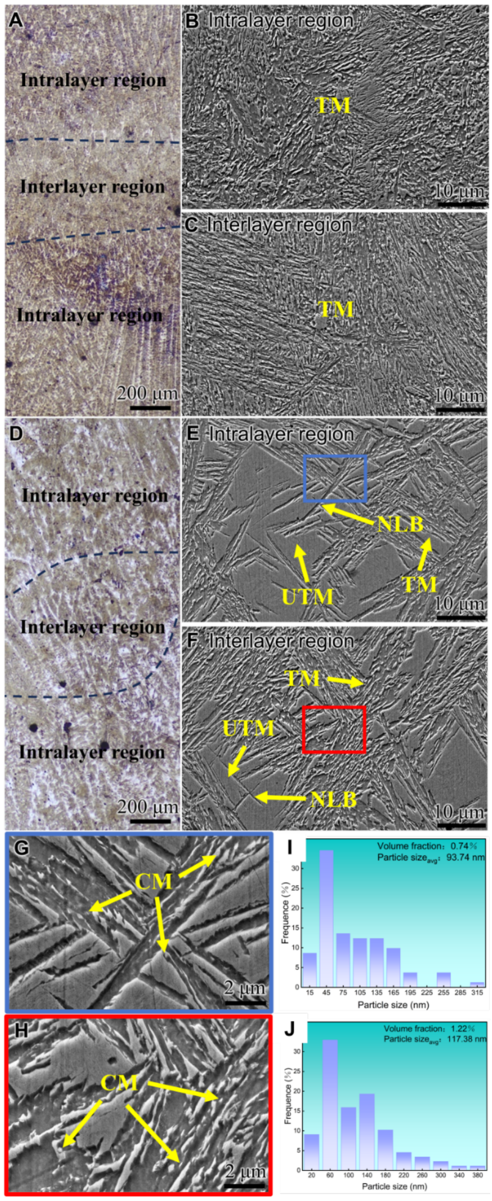

Figure 5. Microstructural differences between the intralayer and interlayer regions at different interlayer temperatures. (A) Optical microscopy overview (scale bar = 200 μm; magnification = 50×), (B) intralayer microstructure (scale bar = 10 μm; magnification = 2,000×), and (C) interlayer microstructure of the sample fabricated at 200 °C (scale bar = 10 μm; magnification = 2,000×). (D) Optical microscopy overview (scale bar = 200 μm; magnification = 50×), (E) intralayer microstructure (scale bar = 10 μm; magnification = 2,000×), (F) interlayer microstructure (scale bar = 10 μm; magnification = 2,000×), (G) magnified view of (E) (scale bar = 2 μm; magnification = 10,000×), (H) magnified view of (F) (scale bar = 2 μm; magnification = 10,000×), (I) CM size distribution corresponding to (G), and (J) CM size distribution corresponding to (H) of the sample fabricated at 300 °C.
Abbreviations: CM: Cementite; NLB: Needle-like bainite; TM: Tempered martensite; UTM: Untempered martensite.

than that in the intralayer region (0.74%). Moreover, the CM in the interlayer region is generally coarser, with an average size of 117.38 nm, which is substantially larger than that in the intralayer region (93.74 nm).

When the interlayer temperature surpasses Ms, notable microstructural heterogeneity is observed between the interlayer and intralayer regions. This heterogeneity is closely related to the complex thermal cycles during the DED-Arc process and the inherent tempering characteristics of 300M steel. When the interlayer temperature is controlled at 200 °C, the deposited layer cools to below Ms during rapid cooling, generating a large amount of UTM. Although the interlayer and intralayer regions undergo different degrees of tempering during subsequent cladding passes, the repeated thermal cycles eventually lead to uniform tempering throughout the entire component. Consequently, both the interlayer and intralayer regions eventually transform into TM, resulting in a homogeneous microstructure.

When the interlayer temperature is increased to 300 °C, which is above Ms, the deposited layer does not transform into martensite upon cooling. Instead, it partially transforms into NLB or remains as austenite, as shown in Figure 6A. The heat input from subsequent cladding layers subjects this layer to more complex thermal cycles. When the peak temperature exceeds the austenitization temperature, this layer undergoes a reverse transformation and reverts to austenite, as shown in Figure 6B. Upon subsequent cooling, when the temperature of this layer drops below Ms, the microstructure begins to transform into UTM, in which carbon atoms remain highly supersaturated with almost no carbide precipitation, as shown in Figure 6C.

As the deposition height increases, the peak temperature transferred to this layer gradually decreases. When the peak temperature falls below the austenitization temperature but stays within the tempering temperature range, the interlayer region near the molten pool undergoes a higher degree of tempering. This leads to a substantial tempering transformation of the previously formed UTM. Supersaturated carbon atoms precipitate from the martensite and combine with iron to form stable CM particles, which subsequently coarsen, leading to an increase in the average CM size. Moreover, the repeated thermal cycles promote further precipitation of carbon atoms, increasing the volume fraction of CM. In contrast, the intralayer region far from the molten pool experiences a lower degree of tempering, so most of the UTM is retained, with only a small amount of fine CM precipitates, as shown in Figure 6D. Therefore, differences in microstructure between the interlayer and intralayer regions are observed.

In summary, when the interlayer temperature exceeds Ms, the spatial variation of thermal exposure during the DED-Arc process leads to different microstructural evolutions. The interlayer region undergoes a complete cycle of austenitization–cooling–sufficient tempering, resulting in a microstructure dominated by TM with a high-volume fraction of coarse CM. In contrast, the intralayer region mainly experiences austenitization–cooling–mild tempering, resulting in a microstructure containing a substantially higher proportion of UTM with a low volume fraction of fine CM.

3.3. Mechanical properties

Figure 7 illustrates the microhardness at different interlayer temperatures. At an interlayer temperature of 200 °C, the average hardness is 428.69 HV, with a relatively uniform distribution. When the interlayer temperature increases to 300 °C, the formation of UTM enhances the solid solution strengthening effect, resulting in an increase in average hardness to 444.34 HV. However, the non-uniform distribution of soft and hard phases at this temperature leads to a notable hardness difference between the interlayer and intralayer regions. A distinct feature of soft/hard zone partitioning is evident: the intralayer region exhibits higher hardness than the interlayer region. The formation of such soft/hard zones is primarily attributed to the differential tempering effects caused by the spatial variation of thermal cycles between the interlayer and intralayer regions.

In addition, factors such as residual stress and elemental segregation may also influence the microstructural evolution of DED-Arc components. However, Sun *et al.*[36] investigated the residual stress distribution in DED-Arc UHSS. The reported residual stress distribution cannot strictly account for the periodic soft/hard zone pattern aligned with the layer-by-layer deposition interfaces. As evidenced by the quantitative microstructural data in Figure 5, this pattern is a typical feature of thermally induced phase transformation and differential tempering, rather than being caused by residual stress distribution. Furthermore, elemental segregation is a common solidification characteristic in additive manufacturing, arising from the uneven distribution of alloying elements during solidification.[37] Nevertheless, the microstructural evolution during the DED-Arc process is dynamic. The same region undergoes multiple phase transformations during subsequent thermal cycles, including austenitization, transformation to UTM, and subsequent tempering. This dynamic evolution has been confirmed in our previous study[10] and is attributed to the influence of thermal cycles rather than compositional variations. Therefore, although residual stress and elemental segregation may play auxiliary

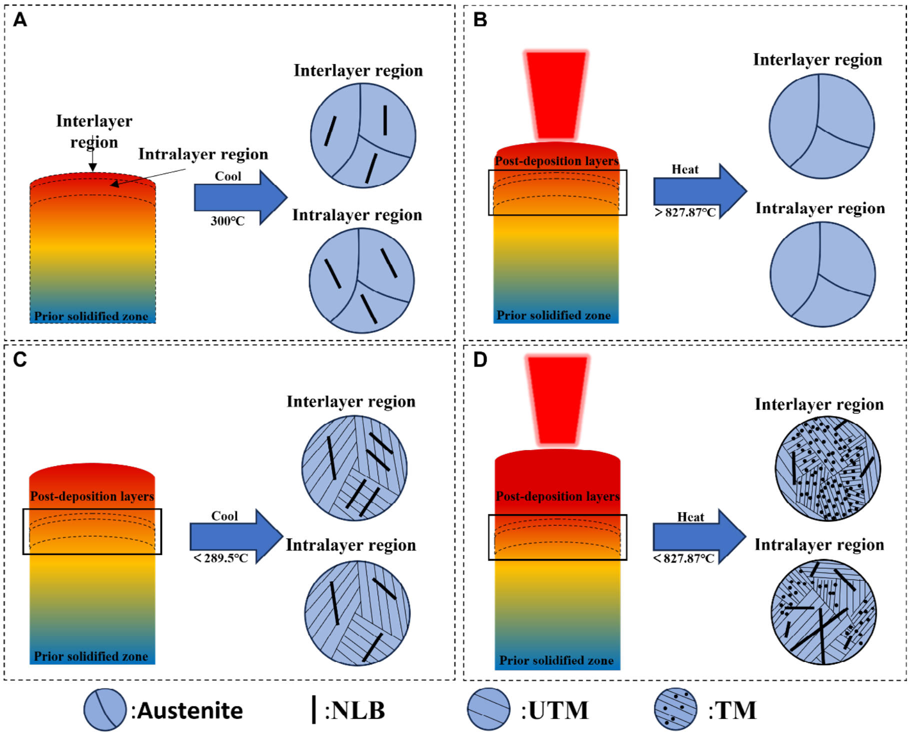

Figure 6. Schematic illustration of the process–microstructure relationship in directed energy deposition–arc 300M steel fabricated at an interlayer temperature of 300 °C. (A) Formation of NLB and austenite after cooling. (B) Thermally induced reaustenitization. (C) Transformation to UTM upon cooling. (D) Microstructural heterogeneity due to differential tempering between intralayer and interlayer regions.
Abbreviations: NLB: Needle-like bainite; TM: Tempered martensite; UTM: Untempered martensite.

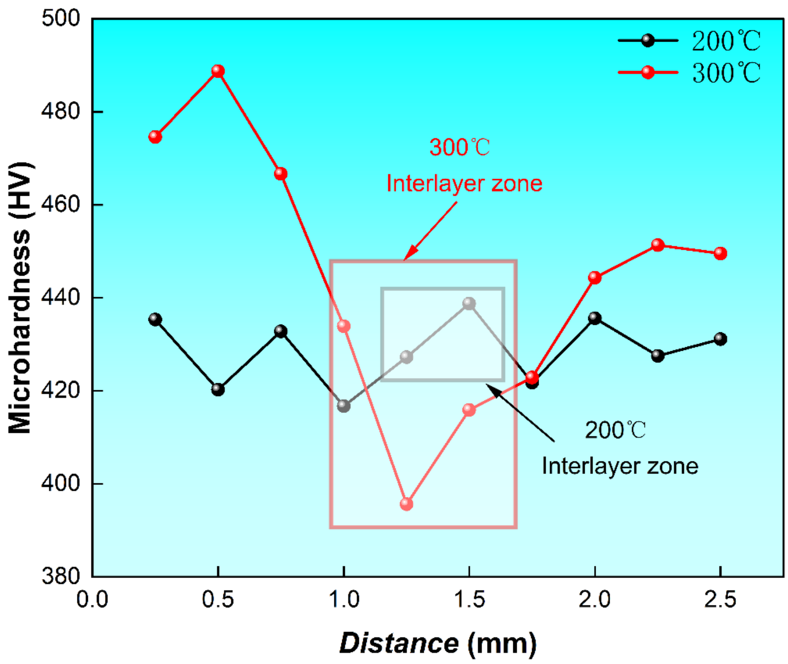

Figure 7. Microhardness of directed energy deposition–arc 300M steel at different interlayer temperatures

roles, the primary mechanism for the formation of soft and hard zones in this study remains the differential tempering caused by the spatial variation of thermal cycles.

Figure 8 illustrates the tensile properties of the deposited components at different interlayer temperatures. With increasing interlayer temperature, the ultimate tensile strength (UTS) increases and the elongation (EL) decreases, while the YS exhibits relatively minor changes. The vertical tensile properties follow a similar trend to the horizontal ones. Notably, when the interlayer temperature reaches 300 °C, the vertical specimens exhibit higher UTS and EL but lower YS than the horizontal specimens, demonstrating a unique mechanical anisotropy.

The changes in mechanical properties can be attributed to the effect of interlayer temperature on the microstructure. When the interlayer temperature increases to 300 °C, UTM forms and NLB subdivides the martensite laths, refining the UTM and thereby increasing the UTS.[38] However, the brittleness of UTM and CM leads to reduced ductility in the material.[39]

Figure 9 illustrates the fracture morphology of the tensile specimens. The fracture behavior is substantially influenced by the interlayer temperature. At an interlayer temperature of 200 °C, the fracture surface is mainly characterized by dimples and quasi-cleavage facets, exhibiting a mixed ductile-to-brittle fracture mode. The horizontal specimens show fewer dimples than the vertical specimens, indicating lower ductility, as shown in Figure 9A and 9C. When the interlayer temperature rises to 300 °C, blocky cleavage facets and CM precipitates are observed on the fracture surface of the horizontal specimens, as shown in Figure 9B, indicating cleavage fracture. In contrast, the vertical specimens exhibit a typical "river-like" quasi-cleavage morphology, as shown in Figure 9D. The failure mode at this interlayer temperature is brittle fracture.

3.4. Mechanical anisotropy

As discussed in **Section 3.3**, the DED-Arc 300M steel exhibits distinct mechanical anisotropy. To further quantitatively analyze the differences in anisotropy, the mechanical anisotropy index was calculated using **Equation 2**:[40]

$$p = \frac{P_{\mathrm{Max}} - P_{\mathrm{Min}}}{P_{\mathrm{Min}}} \tag{2}$$

where p is the anisotropy index, P_{Max} is the maximum tensile property in any direction, and P_{Min} is the minimum tensile property in any direction. The calculated anisotropy index of tensile properties at different interlayer temperatures is shown in Figure 10. According to the anisotropy index, the degree of anisotropy is relatively low at an interlayer temperature of 200 °C. Specifically, at an interlayer temperature of 200 °C, the strength anisotropy of the DED-Arc component is below 1%, which can be considered isotropic.[41] When the interlayer temperature rises to 300 °C, substantial mechanical anisotropy is observed.

During the deposition process, materials undergo repeated rapid heating and cooling cycles, promoting the solidification of molten metals and the formation of a distinct crystallographic texture under substantial temperature gradients. Typically, such a texture is characterized by the preferential growth of grains along specific crystallographic orientations. The strong texture leads to inhomogeneous deformation responses of the material under tensile loading in different directions, thereby resulting in substantial mechanical anisotropy.[42] However, in this study, although a strong texture was observed at both interlayer temperatures of 200 °C and 300 °C (Figure 4G and 4H), the material exhibited isotropic strength and relatively low plastic anisotropy at 200 °C. In contrast, at an interlayer temperature of 300 °C, both strength anisotropy and pronounced plastic anisotropy were present. This indicates that texture has a limited effect on the strength anisotropy of DED-Arc 300M steel.

Microstructural analysis revealed that at an interlayer temperature of 200 °C, the microstructure of the DED-Arc component was uniformly distributed, whereas at 300 °C, it exhibited a pronounced heterogeneous structure. Such microstructural differences induce mechanical anisotropy. At an interlayer temperature of 200 °C, the microstructures of both the interlayer and intralayer regions are uniform and consist entirely of TM. Consequently, the DED-Arc component exhibits low plastic anisotropy but isotropic strength. The YS corresponds to the stress at which the slip systems first reach their critical resolved shear stress (CRSS) and become activated. According to Schmid's law, the CRSS is defined as the minimum shear stress required to initiate plastic slip on a specific slip system. Slip can only be activated when the resolved shear stress acting on a specific slip system exceeds its CRSS, leading to the onset of plastic deformation in the crystal. At an interlayer temperature of 200 °C, a pronounced texture is observed. This leads to a variation in the Schmid factor distribution for specific slip systems, thereby causing anisotropy in the macroscopic CRSS. However, this is contrary to the isotropic behavior observed experimentally. In fact, martensite has a body-centered cubic (BCC) crystal structure with non-planar screw dislocations, often leading to deviations from Schmid's law in BCC materials.[43] Meanwhile, in BCC crystals, multiple slip systems exist. When subjected to

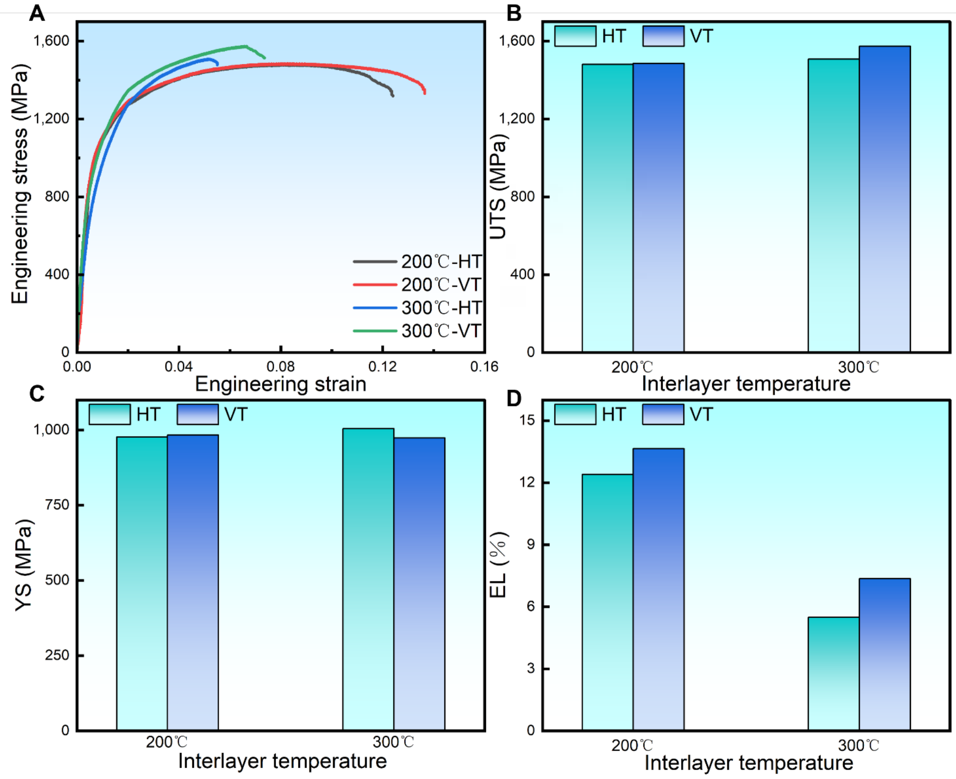

Figure 8. Tensile properties at different interlayer temperatures: (A) Engineering stress–strain curves, (B) UTS, (C) YS, and (D) EL
Abbreviations: EL: Elongation; HT: Horizontal direction; UTS: Ultimate tensile strength; VT: Vertical direction; YS: Yield strength.

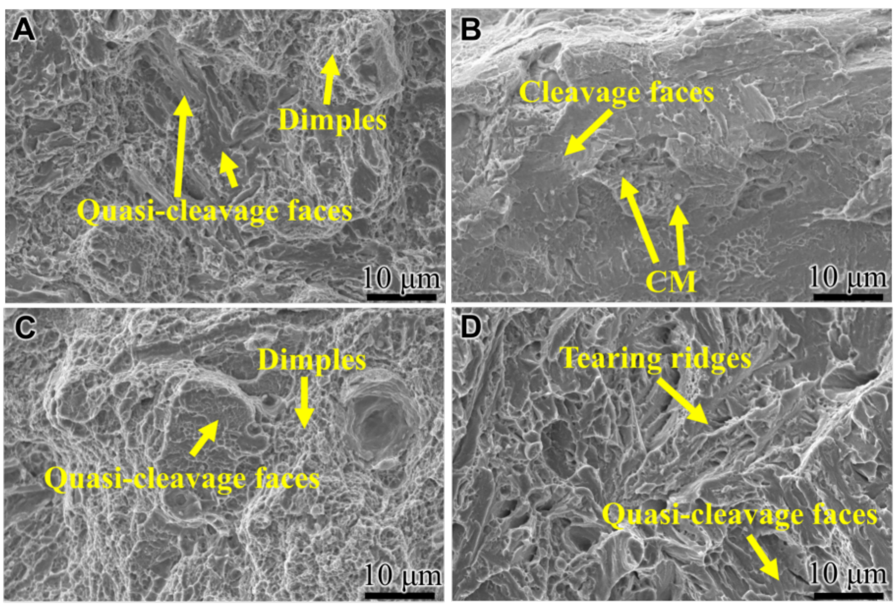

Figure 9. Fracture morphologies of horizontal and vertical tensile specimens fabricated at different interlayer temperatures (scale bar = 10 μm; magnification = 2,000×). (A, B) Horizontal tensile specimen at (A) 200 °C and (B) 300 °C. (C, D) Vertical tensile specimen at (C) 200 °C and (D) 300 °C.
Abbreviation: CM: Cementite.

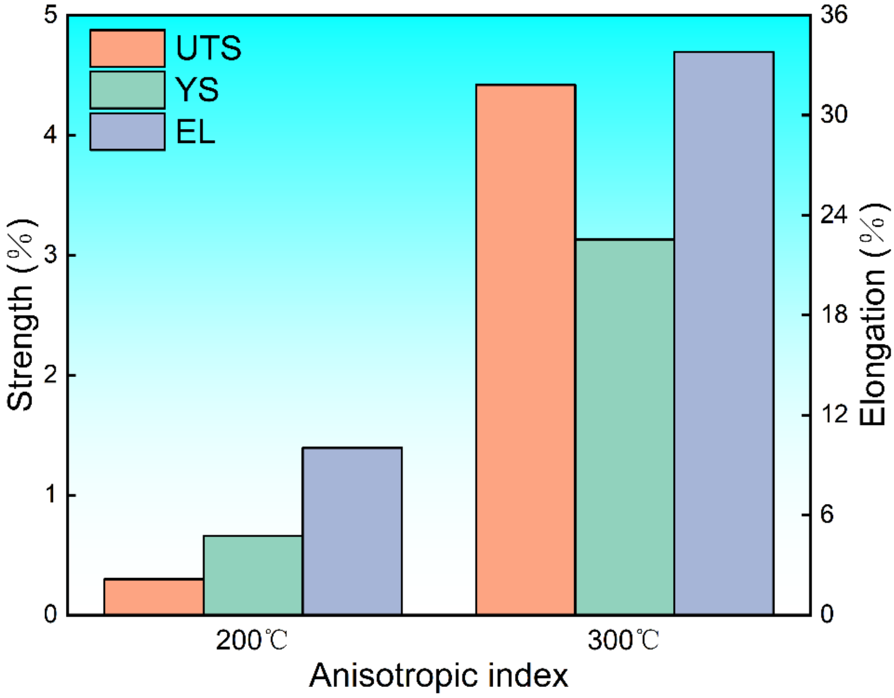

Figure 10. Anisotropy indices of tensile properties at different interlayer temperatures
Abbreviations: EL: Elongation; UTS: Ultimate tensile strength; YS: Yield strength.

uniaxial loading along different directions, at least one favorable slip system with a comparable CRSS is generally available.[44] Furthermore, the polycrystalline nature of the material introduces more complex local stress states, thereby causing a further deviation from the predictions of Schmid's law.[45] Therefore, describing macroscopic yielding behavior accurately solely based on Schmid's law is challenging.

To effectively correlate the crystallographic orientation with the YS of polycrystalline materials, the Taylor factor (M) is commonly introduced. The Taylor factor describes the relationship between macroscopic deformation and the activation of multiple slip systems required to accommodate strain in polycrystalline materials. It is crucial for analyzing the plastic deformation of polycrystalline materials, and its value depends on the grain orientation and the type of slip systems.[46] The Taylor factor is defined as follows:[47]

$$M = \frac{\sigma_y}{\tau_0} \tag{3}$$

where σ_y is the yield stress and τ_0 is the CRSS. For a material with a pronounced texture, if the M values differ substantially along different loading directions, the contribution of crystallographic texture to YS anisotropy becomes substantial; conversely, if the M values are similar, it tends to be isotropic. Therefore, it is necessary to calculate the distribution of Taylor factors along different loading directions based on EBSD data.

In martensite, two primary slip systems are considered active, namely {110}<111> and {112}<111>, with corresponding CRSS values of 470 MPa and 490 MPa, respectively.[48] These data will be utilized in subsequent calculations. To determine the macroscopic strain state required for the calculation of the Taylor factor, the Lankford coefficient (*r*-value) was measured for the horizontal and vertical tensile specimens. The *r*-value is determined as follows:[49]

$$r = \frac{\varepsilon_w}{\varepsilon_t} = \frac{\ln\left(\frac{w}{w_0}\right)}{\ln\left(\frac{t}{t_0}\right)} \tag{4}$$

where w and w_0 are the final and initial widths of the tensile specimen, respectively, and t and t_0 are the final and initial thicknesses, respectively. To ensure stable plastic deformation and avoid necking effects, the specimen dimensions were measured at an engineering strain of 5%. r_{H} and r_{V} were determined to be 0.84 and 0.73, respectively. Based on these *r*-values obtained from the tensile specimens along different directions, the macroscopic strain tensors for horizontal and vertical tension, denoted as $E_{ij,\mathrm{H}}$ and $E_{ij,\mathrm{V}}$, were determined as follows:

$$E_{ij,\mathrm{H}} = E\begin{bmatrix} -0.46 & 0 & 0 \\ 0 & -0.54 & 0 \\ 0 & 0 & 1 \end{bmatrix}$$

$$E_{ij,\mathrm{V}} = E\begin{bmatrix} 1 & 0 & 0 \\ 0 & -0.42 & 0 \\ 0 & 0 & -0.58 \end{bmatrix}$$

Based on the above strain state and the CRSS of the slip systems, the Taylor factors of martensite obtained from the tensile tests along the horizontal and vertical directions at 200 °C are shown in Figure 11. A higher Taylor factor implies that greater shear stress is required to accommodate plastic deformation. At an interlayer temperature of 200 °C, the average Taylor factors for the horizontal and vertical tensile directions are 2.95 and 2.94, respectively, which are nearly the same. This contributes to the isotropic YS in the two directions, indicating that the material does not exhibit a notable macroscopic directional dependence of the YS at this interlayer temperature.

Regarding the detailed distribution, during horizontal tension, the Taylor factors of martensite are mostly concentrated around 3.2, with a peak value of approximately 3.4. A small fraction of softoriented grains have Taylor factors ranging from 2.1 to 2.4. During vertical tension, the Taylor factor distribution exhibits the highest proportion in the range of 2.9–3.0, with an increased fraction of soft-oriented grains, while a considerable proportion of martensite grains with a peak value of approximately 3.5 are also present. The above results reveal differences in the Taylor factor distributions between the two loading directions. Such distribution differences reflect the different activation of slip systems associated with multiple texture components under different loading directions. Nevertheless, the effects of hard- and soft-oriented grains compensate for each other under different loading directions, resulting in comparable average Taylor factors. This provides a crystallographic explanation for the macroscopic isotropic yield behavior.

After the material is strained beyond the yield point, plastic deformation occurs and dislocations begin to move. At this stage, the pinning effect of precipitates on dislocations is the dominant factor controlling the tensile strength of UHSS.[50,51] At an interlayer temperature of 200 °C, the uniform microstructure and dispersed distribution of carbides result in a similar pinning effect on dislocations during tensile loading along different directions, leading to negligible differences in UTS. Plastic anisotropy arises from variations in the ability to coordinate deformation along different directions.[52] Plastic deformation preferentially occurs along slip planes, and the motion of dislocations within these planes is the primary mechanism of plastic deformation. However, grain boundaries act as obstacles to dislocation motion, thereby hindering plastic deformation.[40] At 200 °C, a strong crystallographic texture is present. Martensite grows epitaxially along the build direction. For vertical specimens, the loading direction is approximately parallel to the grain boundaries, resulting in weaker obstruction to deformation by the grain boundaries, better deformation coordination, and thus higher EL. For horizontal specimens, the loading direction is perpendicular to the grain boundaries. During deformation, dislocations must traverse the grain boundaries, leading to greater deformation resistance and consequently lower EL.

At an interlayer temperature of 300 °C, the Taylor factors for the horizontal and vertical tensile directions were also calculated based on EBSD data. Since the specimens exhibited brittle fracture at an interlayer temperature of 300 °C, the specimen dimensions for the calculation of the r-value were measured at an engineering strain of 4%. The r_{H} and r_{V} were calculated as 1.10 and 1.27, respectively. Based on these r-values, the macroscopic strain tensors for horizontal and vertical tension, denoted as $E_{ij,\mathrm{H}}$ and $E_{ij,\mathrm{V}}$, were determined as follows:

$$E_{ij,\mathrm{H}} = E\begin{bmatrix} -0.52 & 0 & 0 \\ 0 & -0.48 & 0 \\ 0 & 0 & 1 \end{bmatrix}$$

$$E_{ij,\mathrm{V}} = E\begin{bmatrix} 1 & 0 & 0 \\ 0 & -0.56 & 0 \\ 0 & 0 & -0.44 \end{bmatrix}$$

Based on the above macroscopic strain tensor and the CRSS of the relevant slip systems, the Taylor factors for the horizontal and vertical tensile directions at an interlayer temperature of 300 °C were calculated. The results are shown in Figure 12. The average Taylor factors in the two directions are 2.82 and 2.88, respectively, with a negligible difference. However, the YS at this temperature exhibits anisotropy, with the horizontal YS being higher than the vertical one, which contradicts the prediction based on the

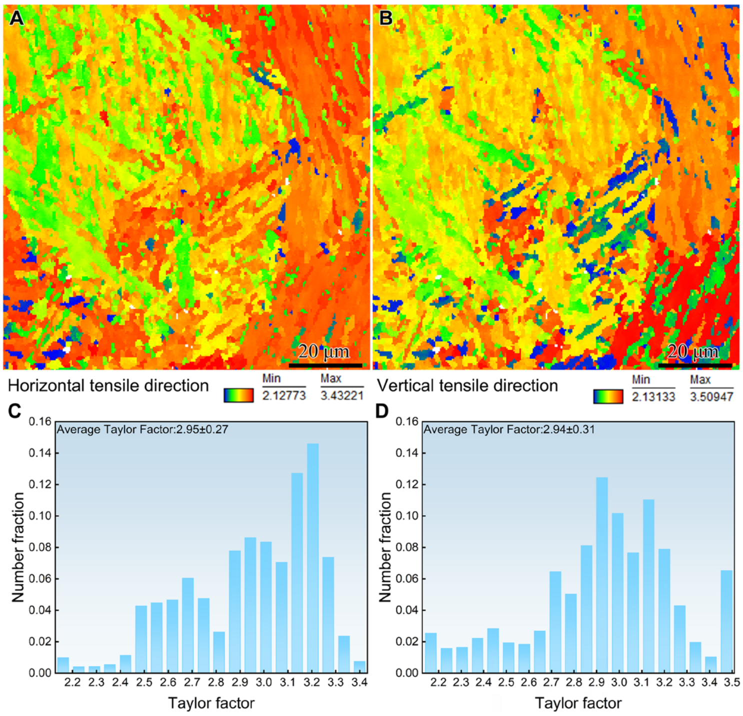

Figure 11. Taylor factors of martensite at an interlayer temperature of 200 °C. (A, B) Taylor factor maps calculated from the initial specimens subjected to tensile deformation along the (A) horizontal and (B) vertical directions (scale bar = 20 μm; magnification = 1,500×). (C, D) Corresponding Taylor factor distribution for the (C) horizontal and (D) vertical directions.

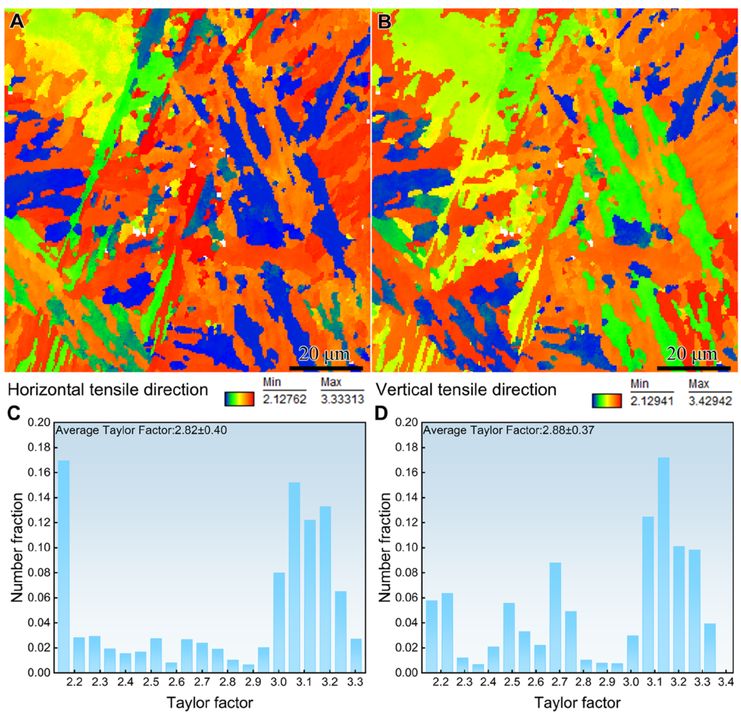

Figure 12. Taylor factors of martensite at an interlayer temperature of 300 °C. (A, B) Taylor factor maps calculated from the initial specimens subjected to tensile deformation along the (A) horizontal and (B) vertical directions (scale bar = 20 μm; magnification = 1,500×). (C, D) Corresponding Taylor factor distribution for the (C) horizontal and (D) vertical directions.

Taylor factor. This indicates that the direction dependence of YS at 300 °C is less influenced by crystallographic orientation effects and should be mainly attributed to microstructural heterogeneity.

The heterogeneous structure, characterized by an uneven distribution of soft and hard microstructural regions between the interlayer and intralayer regions, leads to substantial local hardness variations, thereby forming soft and hard zones. The soft and hard zones exhibit distinctly different deformation behaviors under tensile loading. The soft zones undergo preferential plastic deformation and possess higher ductility, whereas the hard zones provide higher deformation resistance.[24,53,54] Figure 13 illustrates the schematic diagrams of tensile loading for the horizontal and vertical specimens at 300 °C.

For the horizontal specimens (with the loading direction parallel to the scanning direction), the alternating stacking direction of the soft and hard zones is perpendicular to the tensile direction, resulting in strong mechanical constraint during deformation. During tension, the soft zones yield first and activate dislocation slip, but their plastic deformation is constrained by the hard zones that remain elastic, preventing homogeneous plastic flow.

For the vertical specimens (with the loading direction parallel to the build direction), the soft and hard zones are arranged in series along the tensile direction. The soft zones are less constrained by the hard zones, resulting in more localized plastic deformation. Therefore, the horizontal specimens exhibit higher YS. With increasing deformation, the work hardening effect gradually becomes pronounced. Subsequently, CM contributes to strengthening by impeding dislocation motion through precipitation strengthening, thereby enhancing the UTS. Since CM is a hard, non-shearable precipitate phase and maintains an incoherent relationship with the matrix, this mechanism can be described by the Orowan equation:[55,56]

$$\Delta\sigma_{\text{Orowan}} = M_0 \frac{Gb}{2\pi\sqrt{1-v}} \frac{\ln\frac{\bar{d}}{b}}{\bar{d}\left(\sqrt{\frac{\pi}{4f}}-1\right)} \tag{5}$$

where M_0 is the strengthening coefficient, G is the shear modulus of the matrix, b is the Burgers vector, v is Poisson's ratio, and $\bar{d}$ and f are the average size and volume fraction of the CM particles, respectively. **Equation 5** shows that the Orowan strengthening increment $\Delta\sigma_{\text{Orowan}}$ is closely related to $\bar{d}$ and f. To quantitatively compare the Orowan strengthening contributions of the interlayer and intralayer regions, a geometric factor F is defined as follows:

$$F = \frac{\ln\frac{\bar{d}}{b}}{\bar{d}\left(\sqrt{\frac{\pi}{4f}}-1\right)} \tag{6}$$

This factor comprehensively reflects the influence of CM particle size and volume fraction on Orowan strengthening. Based on the quantitative analysis shown in Figure 5I and 5J, the interlayer region (soft zone) has an average CM size of 117.38 nm and a volume fraction of 1.22%, while the intralayer region (hard zone) has a smaller average size of 93.74 nm and a lower volume fraction of 0.74%. Substituting these values into the geometric factor F yields a ratio of $F_{\text{inter}} / F_{\text{intra}} \approx 1.10$. This result indicates that although the CM particles in the interlayer region are coarser (117.38 nm vs. 93.74 nm), which would reduce the Orowan strengthening effect, their volume fraction (1.22%) is markedly higher than that in the intralayer region (0.74%). The strengthening contribution from the increased volume fraction outweighs the reduction caused by particle coarsening. Consequently, the Orowan strengthening effect in the interlayer region is approximately 10% higher than that in the intralayer region. Since the vertical tensile specimens, extracted along the build direction, are loaded along a direction that engages a greater proportion of interlayer regions, their overall Orowan strengthening contribution is greater. Therefore, the vertical specimens exhibit a higher UTS.

To understand the effect of interlayer temperature on plasticity, the two interlayer temperatures are first compared. At 200 °C, a strong crystallographic texture (maximum intensity of 10.93) exists, yet the plastic anisotropy is only 10.04%, as shown in Figure 10. This demonstrates that texture alone induces only a relatively modest anisotropy. At 300 °C, the maximum texture intensity increases slightly to 13.70, but the plastic anisotropy increases dramatically to 33.94%. Such a disproportionate increase cannot be explained by the modest texture enhancement alone. The dominant role in this substantial enhancement is played by the heterogeneous structure that forms exclusively at 300 °C, although the slightly stronger texture may also play a secondary role.

The effect of the heterogeneous structure is determined by the spatial arrangement of the soft and hard zones relative to the loading direction. In the vertical specimens, the soft and hard zones are arranged in series along the tensile direction, allowing the soft zones to accommodate a large plastic strain and thus exhibiting better deformation compatibility. In contrast, the soft zones in the horizontal specimens are strongly constrained by the hard zones, making it difficult to adequately accommodate plastic

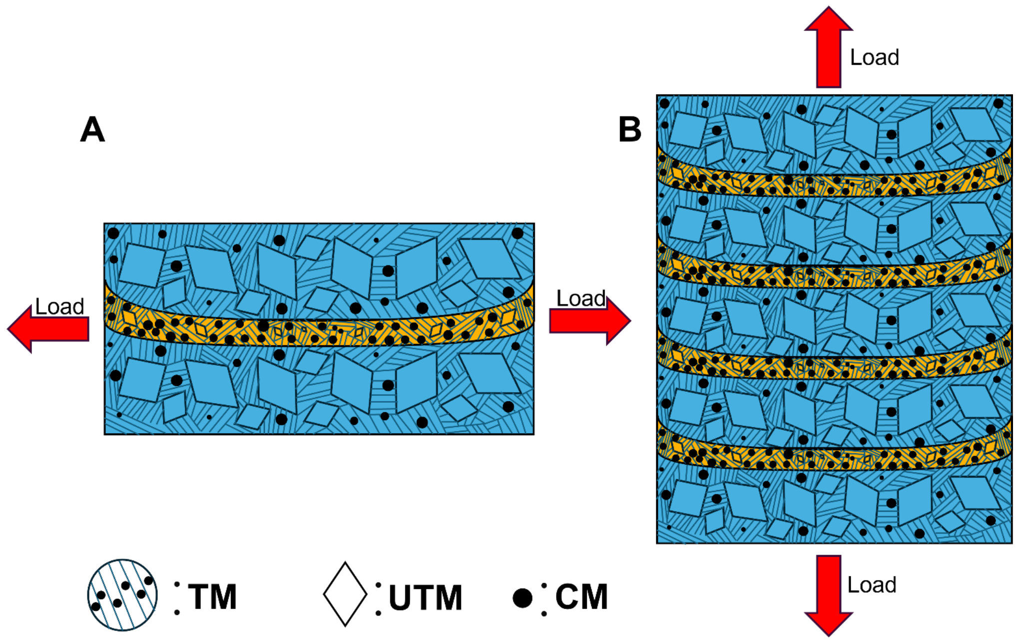

Figure 13. Schematic diagrams of the loading conditions applied to the tensile specimens at an interlayer temperature of 300 °C: (A) Horizontal tensile specimen and (B) vertical tensile specimen
Abbreviations: CM: Cementite; TM: Tempered martensite; UTM: Untempered martensite.

deformation. Moreover, as the horizontal tensile load direction is perpendicular to the direction of heterogeneous structure stacking, brittle fracture dominated by the soft/hard interfaces is more likely to occur, further limiting the ductility of the horizontal specimens.[57]

In summary, the plastic anisotropy observed at 300 °C is mainly influenced by the heterogeneous structure, with texture playing a secondary contributing role.

4. Conclusion

(i) When the interlayer temperature is below Ms, the DED-Arc 300M steel predominantly exhibits uniform microstructure of TM with DC. When the interlayer temperature exceeds Ms, the microstructure evolves into a heterogeneous structure, characterized by soft/hard zones resulting from the uneven distribution of soft phases (TM and NLB) and hard phases (UTM). Moreover, the volume fraction and size of CM in the interlayer region are significantly higher than those in the intralayer region.

(ii) When the interlayer temperature rises from below Ms to above Ms, the UTS increases, the EL decreases, and the YS shows little change. The fracture mode transforms from mixed ductile-brittle to brittle fracture. Correspondingly, the mechanical anisotropy characteristics undergo a marked transition: from isotropic strength and higher elongation in the vertical direction than in the horizontal direction, to vertical specimens exhibiting both higher UTS and EL but lower YS than horizontal specimens.

(iii) When the interlayer temperature is below Ms, the anisotropy of DED-Arc 300M steel is governed by crystallographic orientation effects within the uniform microstructure. When the interlayer temperature exceeds Ms, microstructural heterogeneity becomes the dominant factor, characterized by alternating stacking of soft and hard zones, which leads to different deformation behaviors when stretched along different directions and variations in the Orowan strengthening mechanism.

Acknowledgments

None.

Funding

This work was supported by the National Natural Science Foundation of China (Grant No. 52564058 and 52305373) and the Jiangxi Provincial Natural Science Foundation (Grant No. 20252BAC240335).

Conflict of interest

The authors declare they have no competing interests.

Author contributions

Conceptualization: Mingjie Zhao
Formal analysis: Junyang Tu, You Li
Investigation: Junyang Tu, An Lu
Methodology: Mingjie Zhao, Lihong Jiang
Supervision: Zhenghua Guo
Visualization: Junyang Tu
Writing–original draft: Junyang Tu, Mingjie Zhao
Writing–review & editing: Mingjie Zhao

Ethics approval and consent to participate

Not applicable.

Consent for publication

Not applicable.

Availability of data

The raw and processed data are not currently available for public sharing due to ongoing research activities.

References

1. Bai Y, Zhang S, Yan Q, Zhao C, Zhan J. Enhanced strength of A131 steel via heterostructures induced by laser-directed energy deposition. *Mater Sci Add Manuf*. 2025;4(3):025220038.

   doi: 10.36922/MSAM025220038

2. Zhao M, Jiang L, Li C, *et al*. Flow characteristics and hot workability of a typical low-alloy high-strength steel during multi-pass deformation. *Int J Miner Metall Mater*. 2024;31(2):323-336.

   doi: 10.1007/s12613-023-2736-0

3. Zhao M, Li C, Jiang L, *et al*. Hot workability of a typical ultrahigh strength steel during the isothermal forging process. *Met Mater Int*. 2023;30(4):1055-1071.

   doi: 10.1007/s12540-023-01560-1

4. Li K, Yang TB, Gong N, *et al*. Additive manufacturing of ultra-high strength steels: A review. *J Alloys Compd*. 2023;965:171390.

   doi: 10.1016/j.jallcom.2023.171390

5. Sandua X, Arbizu E, Rodríguez A, Veiga F, Martín MÁ, Rivero PJ. Influence of laser power and hatch spacing on the mechanical properties of AlSi10Mg processed by selective laser melting. *Mater Sci Add Manuf*. 2026;5(2):026040008.

   doi: 10.36922/MSAM026040008

6. Gain S, Veeman D. A review on advances and challenges in wire arc additive manufacturing: Process parameters, microstructural evolution and material performance across alloys. *J Alloys Compd*. 2025;1029:180735.

   doi: 10.1016/j.jallcom.2025.180735

7. Yang L, Yi H, Jia L, Zhang W, Cao H. Achieving collaborative improvement of strength and plasticity of wire arc additive manufactured Ti-6Al-4V titanium alloy via ultrasonic vibration and heat treatment. *Appl Mater Today*. 2026;48:103040.

   doi: 10.1016/j.apmt.2025.103040

8. Zhang H, Li R, Liu J, et al. State-of-art review on the process-structure-properties-performance linkage in wire arc additive manufacturing. *Virtual Phys Prototyp*. 2024;19(1).

   doi: 10.1080/17452759.2024.2390495

9. Wang X, Deng J, Zhao R, Shen L, Wang Z. Compressive response and energy absorption of 3D-printed cellular structures: advances and challenges. *Virtual Phys Prototyp*. 2026;21(1).

   doi: 10.1080/17452759.2026.2638085

10. Guo Z, Lu A, Zhao M, Jiang L, Wang G. Effects of bainite transformation on mechanical properties of 300 M ultra-high strength steel fabricated by power plasma arc additive manufacturing. *Materialia*. 2025;44:102586.

    doi: 10.1016/j.mtla.2025.102586

11. Zhang J, Fan J, Xu J, ang D, Peng Y, Wang K. The effect of heat input on the microstructure and mechanical properties of 18Ni 300 maraging steel fabricated by arc directed energy deposition. *Mater Sci Eng A*. 2023;884:145545.

    doi: 10.1016/j.msea.2023.145545

12. Lyu Z, Sato YS, Xu W, *et al*. Simultaneous enhancements of strength and ductility of wire arc additive manufactured 174PH steel via intrinsic heat treatment. *J Mater Process Technol*. 2023;321:118149.

    doi: 10.1016/j.jmatprotec.2023.118149

13. Xiong Y, Wen D, Zheng Z, Sun C, Xie J, Li J. Effect of heat treatment on microstructure and mechanical properties of directed energy deposition-Arc 300M steel. *Mater Charact*. 2023;198:112756.

    doi: 10.1016/j.matchar.2023.112756

14. Li Y, Xiong Y, Zhao M, *et al*. Synergistic enhancement of strength and ductility for plasma arc additive manufactured ultrahigh strength steel by a novel heat treatment. *Arch Civ Mech Eng*. 2026;26(3).

    doi: 10.1007/s43452-026-01501-w

15. Dekis M, Tawfik M, Egiza M, Dewidar M. Challenges and developments in wire arc additive manufacturing of steel: a review. *Results Eng*. 2025;26:104657.

    doi: 10.1016/j.rineng.2025.104657

16. Wang C, Lou D, Duan Z, Rong J, Xu B. Structural topology optimization considering multi-source anisotropic failure strength from printing space and material locality. *Comput*

Methods Appl Mech Eng. 2025;446:118309.

doi: 10.1016/j.cma.2025.118309

17. Shi Q, Wang J, Xu X, Liu Y, Wen Z, Yue Z. Temperature-dependent tensile anisotropic behavior of WAAM-TC4 dual-phase titanium alloy: Microstructural evolution, deformation mechanisms, and fracture characteristics. *Mater Sci Eng A*. 2025;943:148748.

doi: 10.1016/j.msea.2025.148748

18. Blinn B, Hassel T, Viebranz VF, Beck T, Maier HJ. Influence of the grain orientation and δ-ferrite on the cyclic deformation behavior of an austenitic CrNi steel manufactured by wire and arc additive manufacturing. *Mater Sci Eng A*. 2023;870:144612.

doi: 10.1016/j.msea.2023.144612

19. Akbarzadeh Chiniforoush E, Zargari HH, Jandaghi MR, Moverare J, Warsi R, Gür CH. A sustainable strategy for wire arc additive manufacturing of high-performance duplex stainless steel: Microstructural refinement and mechanical anisotropy reduction. *Mater Sci Eng A*. 2025;943:148785.

doi: 10.1016/j.msea.2025.148785

20. Palmeira Belotti L, van Dommelen JAW, Geers MGD, Ya W, Hoefnagels JPM. Influence of the printing strategy on the microstructure and mechanical properties of thick-walled wire arc additive manufactured stainless steels. *J Mater Process Tech*. 2024;324:118275.

doi: 10.1016/j.jmatprotec.2023.118275

21. Sun L, Jiang F, Huang R, Yuan D, Guo C, Wang J. Anisotropic mechanical properties and deformation behavior of low-carbon high-strength steel component fabricated by wire and arc additive manufacturing. *Mater Sci Eng A*. 2020;787:139514.

doi: 10.1016/j.msea.2020.139514

22. Chen W, Cao H, Zhu L. Heterogeneous microstructure and anisotropic mechanical properties of reduced activation ferritic/martensitic steel fabricated by wire arc additive manufacturing. *Nucl Mater Energy*. 2022;33:101261.

doi: 10.1016/j.nme.2022.101261

23. Tu Y, Zheng D, Li Z, Zhang C, Gong X. Microstructure and mechanical properties of Mg-12Gd-3Y-0.4Zr magnesium alloy with layered heterogeneous microstructure fabricated by wire arc additive manufacturing. *J Alloys Compd*. 2025;1037:182210.

doi: 10.1016/j.jallcom.2025.182210

24. Lyu Z, Sato YS, Tokita S, Zhao Y, Jia J, Wu A. Microstructural distribution and anisotropic tensile behavior in a 2Cr13 martensitic stainless steel thin wall fabricated by wire arc additive manufacturing. *Mater Today Commun*. 2021;29:102870.

doi: 10.1016/j.mtcomm.2021.102870

25. Zhai W, Wu N, Zhou W. Effect of interpass temperature on wire arc additive manufacturing using high-strength metal-cored wire. *Metals*. 2022;12(2):212.

doi: 10.3390/met12020212

26. Xiong Y, Wen D, Zheng Z, Li J. Effect of interlayer temperature on microstructure evolution and mechanical performance of wire arc additive manufactured 300M steel. *Mater Sci Eng A*. 2022;831:142351.

doi: 10.1016/j.msea.2021.142351

27. Wei S, Wang P, Zhang L, Ramamurty U. Grain morphologies in additively manufactured alloys: From solidification fundamentals to advanced microstructure control. *J Mater Sci Technol*. 2025;235:133-145.

doi: 10.1016/j.jmst.2025.02.033

28. Gao P, Fan J, Cai B, *et al*. Effect of interlayer temperature on the microstructure and mechanical properties of new Co-Free maraging steel fabricated by arc-based directed energy deposition. *Mater Charact*. 2025;222:114851.

doi: 10.1016/j.matchar.2025.114851

29. Salahi S, Nemani AV, Ghaffari M, Lunde J, Nasiri A. On microstructure, crystallographic orientation, and corrosion properties of wire arc additive manufactured 420 martensitic stainless steel: Effect of the inter-layer temperature. *Addit Manuf*. 2021;46:102157.

doi: 10.1016/j.addma.2021.102157

30. Liu F, Lin X, Song M, *et al*. Effect of tempering temperature on microstructure and mechanical properties of laser solid formed 300M steel. *J Alloys Compd*. 2016;689:225-232.

doi: 10.1016/j.jallcom.2016.07.276

31. Chen R, Zheng Z, Li N, Li J, Feng F. In-situ investigation of phase transformation behaviors of 300M steel in continuous cooling process. *Mater Charact*. 2018;144:400-410.

doi: 10.1016/j.matchar.2018.07.034

32. Franceschi M, Morales-Rivas L, Cordova-Tapia E, Jimenez JA, Dabalà M, Garcia-Mateo C. Study of bainite and martensite tempering in a medium C high Si steel. microstructural disparities and equilibrium convergence. *J Mater Res Technol*. 2024;32:2931-2944.

doi: 10.1016/j.jmrt.2024.08.141

33. Hu Z, Hua L, Ni M, Ji F, Qin X. Microstructure and mechanical properties of directed energy deposition-arc/wire bimetallic hierarchical structures of hot-working tool steel and martensitic stainless steel. *Addit Manuf*. 2023;67:103495.

doi: 10.1016/j.addma.2023.103495

34. Li M, Zhang W, Zhou Z, *et al*. Effect of the interlayer temperature on microstructure and mechanical behavior of the high-strength low-alloy steel manufactured by the wire arc additive manufacturing. *Mater Today Commun*.

2025;46:112845.

doi: 10.1016/j.mtcomm.2025.112845

35. Wang X, Li J, Huang S, *et al*. Elimination mechanism of the anisotropy of additively manufactured alloys in high temperature mechanical properties by HG-S2A treatment. *J Alloys Compd*. 2025;1044:184377.

doi: 10.1016/j.jallcom.2025.184377

36. Sun J, Ma N, Deng D, Dilger K. Generation mechanism and distribution characteristics of residual stresses in wire-arc additively manufactured ultra-high strength steel components. *J Mater Res Technol*. 2025;38:6244-6259.

doi: 10.1016/j.jmrt.2025.09.059

37. Turnali A, Kibaroglu D, Evers N, et al. Segregation-guided alloy design via tailored solidification behavior. *Mater Today Adv*. 2025;25:100549.

doi: 10.1016/j.mtadv.2024.100549

38. Feng L, Gao J, Liu F, Huang C, Zheng Y. Effect of grain orientation on microstructure and mechanical properties of laser welded joint of additive manufactured 300M steel. *Mater Today Commun*. 2023;35:105497.

doi: 10.1016/j.mtcomm.2023.105497

39. Jing G, Huang W, Yang H, Wang Z. Microstructural evolution and mechanical properties of 300M steel produced by low and high power selective laser melting. *J Mater Sci Technol*. 2020;48:44-56.

doi: 10.1016/j.jmst.2019.12.020

40. Mishra NK, Ajay V, Nakrani J, Shrivastava A. Influence of dwell time on mechanical and microstructural anisotropy of additively manufactured SS 316 L: Experimental and numerical investigation. *J Manuf Process*. 2025;145:600-615.

doi: 10.1016/j.jmapro.2025.04.072

41. Liu X, Liu ZT, Zhang SY, *et al*. Isotropic high strength Al-Mg-Si-Zn-Cu alloy fabricated by wire-arc additive manufacturing via Ti nanoparticles addition. *Mater Charact*. 2026;233:116148.

doi: 10.1016/j.matchar.2026.116148

42. Palmeira Belotti LP, van Dommelen JAW, Geers MGD, Goulas C, Ya W, Hoefnagels JPM. Microstructural characterisation of thick-walled wire arc additively manufactured stainless steel. *J Mater Process Technol*. 2022;299:117373.

doi: 10.1016/j.jmatprotec.2021.117373

43. Tian C, Ponge D, Christiansen L, Kirchlechner C. On the mechanical heterogeneity in dual phase steel grades: Activation of slip systems and deformation of martensite in DP800. *Acta Mater*. 2020;183:274-284.

doi: 10.1016/j.actamat.2019.11.002

44. Isavand S, Rao PS, Bondarev A, et al. Integrating micropillar compression testing and crystal plasticity modelling to unravel slip system activity and deformation mechanisms in P91 steel. *Mater Sci Eng A*. 2025;942:148659.

doi: 10.1016/j.msea.2025.148659

45. Ng KS, Ngan AHW. Breakdown of Schmid's law in micropillars. *Scr Mater*. 2008;59(7):796-799.

doi: 10.1016/j.scriptamat.2008.06.019

46. Shen JH, Li YL, Wei Q. Statistic derivation of taylor factors for polycrystalline metals with application to pure magnesium. *Mater Sci Eng A*. 2013;582:270-275.

doi: 10.1016/j.msea.2013.06.025

47. Sarkar A, Sanyal S, Bandyopadhyay TK, Mandal S. Implications of microstructure, taylor factor distribution and texture on tensile properties in a Ti-added Fe-Mn-Al-Si-C steel. *Mater Sci Eng A*. 2019;767:138402.

doi: 10.1016/j.msea.2019.138402

48. Jia N, Cong ZH, Sun X, *et al*. An in situ high-energy X-ray diffraction study of micromechanical behavior of multiple phases in advanced high-strength steels. *Acta Mater*. 2009;57(13):3965-3977.

doi: 10.1016/j.actamat.2009.05.002

49. Wronski S, Wierzbanowski K, Jędrychowski M, *et al*. Microstructure evolution of titanium after tensile test. *Mater Sci Eng A*. 2016;656:1-11.

doi: 10.1016/j.msea.2015.12.041

50. Gao P, Jing G, Lan X, *et al*. Effect of heat treatment on microstructure and mechanical properties of Fe–Cr–Ni–Co–Mo maraging stainless steel produced by selective laser melting. *Mater Sci Eng A*. 2021;814:141149.

doi: 10.1016/j.msea.2021.141149

51. Yin S, Chen C, Yan X, *et al*. The influence of aging temperature and aging time on the mechanical and tribological properties of selective laser melted maraging 18Ni-300 steel. *Addit Manuf*. 2018;22:592-600.

doi: 10.1016/j.addma.2018.06.005

52. Otani Y, Takata N, Suzuki A, Kobashi M, Kato M. Microstructural origin of anisotropic tensile ductility of Al-Si alloy manufactured by laser powder bed fusion. *Scr Mater*. 2023;226:115259.

doi: 10.1016/j.scriptamat.2022.115259

53. Jing G, Wang Z. Influence of molten pool mode on microstructure and mechanical properties of heterogeneously tempered 300M steel by selective laser melting. *J Mater Process Technol*. 2021;296:117188.

doi: 10.1016/j.jmatprotec.2021.117188

54. Wang H, Zhang J, Liu Y, *et al*. Achieving high strength and low modulus titanium alloy with non-uniform multiscale heterogeneous microstructures. *J Mater Sci Technol*.

2026;264:151-162.

doi: 10.1016/j.jmst.2025.11.026

55. Jing G, Wang Z. Defects, densification mechanism and mechanical properties of 300M steel deposited by high power selective laser melting. *Addit Manuf*. 2021;38:101831.

doi: 10.1016/j.addma.2020.101831

56. Ma K, Wen H, Hu T, *et al*. Mechanical behavior and strengthening mechanisms in ultrafine grain precipitation-strengthened aluminum alloy. *Acta Mater*. 2014;62:141-155.

doi: 10.1016/j.actamat.2013.09.042

57. Yu Q, Zhang Y, Jia Z, Huang L, Geng L. Synergistic effect of aluminum distribution and in-situ annealing on layered microstructure formation: Microstructural evolution and mechanical anisotropy mechanisms in EBM-fabricated Ti-48Al-2Cr-2Nb. *Mater Sci Eng A*. 2026;949:149383.

doi: 10.1016/j.msea.2025.149383